Metallurgical and Materials Engineering *Research paper*
https://doi.org/10.56801/MME869

MATHEMATICAL AND EXPERIMENTAL EXAMINATION OF THE EFFECT OF THE STEPPED PIN TOOL PROFILE ON THE CHARACTERIZATION OF AA 6061-T6 UNDERWATER FRICTION STIR WELDING

Kiran Wakchaure [*], A. G. Thakur

Sanjivani College of Engineering, Kopargaon, (SPPU, Pune) Maharashtra, 423603, India

Received 25.07.2022
Accepted 29.12.2022

Abstract

This research paper presents the mathematical model to design a stepped pin profile tool and its durability index. A mathematical model is being developed by considering tools that should generate the same heat as conventional conical tools and stepped tools by varying the shoulder to pin diameter ratio (D/d). Aluminum alloy AA6061-T6 with a thickness of 6 mm fabricated using a butt-type weld configuration and newly developed conical stepped pin profile tools with water as a cooling medium. The result shows that a conical stepped tool shows better mechanical properties of the welded joints compared with a conventional conical tool. When compared to other stepped conical pin profile tools, one with a (D/d) of 3 has superior mechanical and microstructural properties and as the D/d ratio increases, the tool pin durability index falls.

Keywords: underwater friction stir welding; AA6061-T6; tool pin profile; conical tool; conical stepped pin tool profile.

Introduction

Friction stir welding (FSW) is one of the modern welding processes, which was invented by Welding Institute, UK in 1991. It's an environment friendly solid state joining process to fulfil the increasing demand for efficient and lightweight structures to save the total cost and the weight [1]. Earlier, FSW was limited to laboratory experiments to weld to 2xxx and 7xxx series aluminum alloy, which are difficult to weld by conventional fusion welding techniques. As the research progresses in FSW, this welding process starts gaining popularity to weld almost all the types of engineering material and its alloys like

[*]Corresponding author: Kiran Wakchaure, *kiran.wakchaure@yahoo.com*

Aluminum, steel, titanium, Nickel, Plastic, etc., with similar or dissimilar material joints with different welding configurations [2].

In recent years, the demand for lightweight alloys such as aluminum (Al) alloys has skyrocketed [3]. Because of their high strength, good formability, corrosion resistance, and weight savings, aluminum alloys have been widely used in aerospace, automotive, electronics, and shipbuilding [4]. However, joining these alloys presents significant difficulties. Because fusion welding techniques join materials by melting and solidification, the use of conventional fusion welding techniques for joining such alloys is prone to generating defects such as oxidation, distortion, porosity, and solidification cracks in joints [3]. Materials to be welded in FSW are clamped in specially designed fixtures based on the configuration of welded joints such as a butt joint, lap joint, T joint, and so on. In FSW, non-consumable profile tools with two centrally distinct parts, pin and shoulder, are used. The special purpose machine tool has the tool mounted on a spindle, and the fixture is mounted on the bed. A rotating tool pin can be inserted into abutting edges of welded material by making sure the shoulder touches the top surface of the material [2]. Due to material plastic deformation and friction between the top surface and the shoulder, a rotary pin piercing inside the joint line generates heat. It is another heat source responsible for raising the temperature of the material at the joint in order to melt it below its melting point temperature. As the material softens, the tool moves in the longitudinal direction along the weld line at a sufficient speed. The tool traverses cause severe plastic deformation and mixing of the plasticized flow on both sides of the material during welding. Also, transport the material from the tool's leading edge to the tool's trailing edge [5]. The tool shoulder prevents material from escaping from the weld and ensures the welding of two materials. Coalescence of pin driven flow and material driven flow in weld nugget form strong welding joint by friction stir welding process shown in Figure 1.

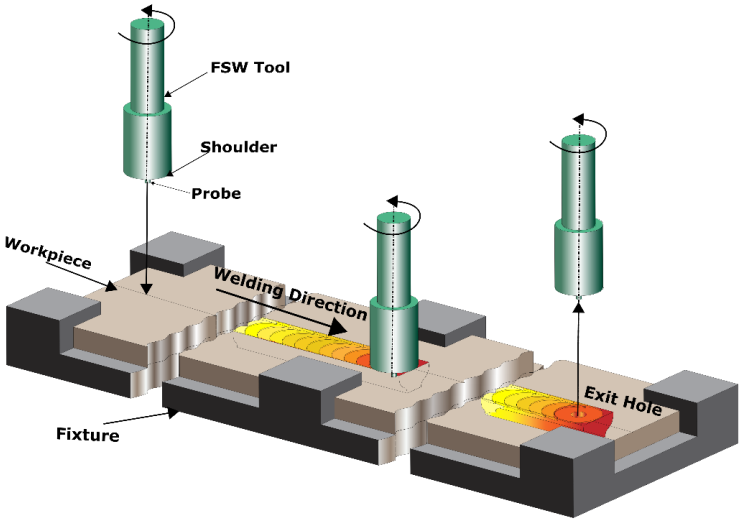

Fig. 1. Schematic of friction stir welding process.

The process parameters tool geometry, tool rotation speed, tool traverse speed, tool tilt angle, axial force, and plunge depth affect the joint integrity and material characterization [6-9]. In friction stir welding, a profiled tool plays a vital role in heat generation due to friction and plastic deformation, material plastic flow in the nugget zone, the power required to perform FSW, and welded joints' integrity with proper materials selection of other processes parameters.

Elongovan et al. [10] considered the influence of different tool profiles (straight cylindrical, tapered cylindrical, threaded cylindrical, triangular, and square tool pin) on the mechanical properties of the FSW of AA2219. Their research reveals that pulsating action due to the square tool pin profile gives defect-free and improved mechanical properties compared with other tool pin profiles. Also, the mechanical properties of a tapered cylindrical tool were just above those of a straight cylindrical tool. Kumar and Raju [11] examined the effect of tool pin geometries polygonal tool pins on the microstructure and mechanical characterization of the FSW of copper. The result shows that the mechanical and microstructural properties show variation concerning tool pin profiles.

Banik et al. [12] discovered that conical threaded tools with higher tilt angles significantly improve the mechanical and microstructural properties of conical tools. *Suresha et al.* [13] discovered that a conical tool pin profile outperforms a square tool pin profile for FSW of AA 7075 of 5 mm thickness. For FSW of bimetallic Al-Cu joints, *Beygi et al.* [14] discovered that conical threaded tools create more downward material flow to avoid micro voids than threaded cylindrical and pyramidal tools. When compared to straight pin tools, *Malik et al.* [15] discovered that frustum-type tool pins consume less power and help to reduce defects. *Kumar et al.* [16] developed special experimentation to investigate the impact of tool pin profile on weld formation. The results show that weld formation occurs in FSW due to the convergence of pin-driven and shoulder-driven flow. *Malik et al.* [17] used plasticine and FEA modeling to conclude that square and triangular tool pin profiles aid in mixing in the nugget zone due to their greater action. The transportation of material lumps formed around the tool with faces causes intense mixing in the nugget zone. *Gadakh et al.* [18] created an analytical and numerical heat generation model for taper cylindrical, taper polygonal pin tools with sides ranging from 3 to 6. The results show that as the number of sides on a polygonal tool pin increases from triangular to square, the peak temperature begins to decrease, and the lowest temperature is generated for a cylindrical taper tool.

Ramaiyan et al. [19] investigated the effects of stepped cylindrical and stepped square pins on the mechanical properties of AZ31B magnesium alloy submerged FSW. The stepped tool with a square pin reveals more recrystallization with refined grains in the nugget zone without any defects when compared to its counterparts. When welding 6 mm of 6061 aluminum alloy, *Prakash et al.* [20] discovered that the stepped conical pin tool and the cylindrical-conical pin tool produce finer gains than the cylindrical and conical pin tools. Welded specimens with a conical stepped tool exhibit superior mechanical properties in terms of tensile strength and percentage elongation. *Arab et al.* [21] discovered that the coefficient of friction stepped tool profiles with base material are responsible for grain refinement in the nugget zone as well as improved mechanical properties when compared to conventional tools. *Xu et al.* [22] discovered that stepped pin tool profiles can achieve a stable interfacial morphology for friction stir lap welding joints of aluminum alloy under various process parameters. *Emamian et al.* [23]

investigated the effects of square, conical, threaded cylindrical, and stepped conical shapes on temperature and tensile strength in AA 6061 Alloy FSW. Tool pin profiles were discovered to influence microstructure properties, resulting in changes in the mechanical behavior of welded joints. *Salari et al.* [24] discovered that a stepped conical tool pin profile improves the welded joint's integrity and mechanical properties. *Chao et al.* [25] used a FEA approach to investigate the thermal and heat transfer phenomena of FSW without taking heat generation from the material plastic flow into account. The results are in good agreement with the experimental results. *Neto et al.* [26] created an analytical model for heat generation that took partial sliding/sticking contact conditions between tool and workpiece into account. *Nandan et al.* [27] created a three-dimensional numerical model to calculate non-Newtonian viscosity of metal flow while taking temperature-dependent material properties, strain rate, and temperature into account. The calculated thermal history and HAZ geometry closely match the experimental values. *Ji et al.* [28] investigated the effect of tool geometry on the plastic flow behavior of materials in friction stir weld joints.

Khandkar [29] developed a mathematical model that accounts for sticking and sliding contact conditions in conventional heat generation. *Sahlot et al.* [30] used numerical three-dimensional heat transfer to compute the temperature history of the weld zone during FSW of copper material under steady-state conditions and compare it to measured values. *Zhu et al.* [31] used the WELDSIM software tool to develop a numerical model by adapting uncoupled thermal and thermo-mechanical analysis of FSW of 304L stainless steel to study residual stresses and transient temperatures, and experimental results show good agreement with numerical data. *Gadakh et al.* [32] developed an analytical heat generation model for friction stir that takes into account uniform contact shear stress at the tool-workpiece interface. The peak temperatures obtained by modeling are consistent with previous research. *Lammlein et al.* [33] demonstrated experimentally and numerically that an aluminum alloy FSW weld could be produced using a shoulder-less conical tool. Conical tools, due to their shape, can handle changes in the height of the material surface caused by thickness changes. *Shinde et al.* [34] used the full factorial method with mixed levels of process parameters in their experimental study. The results show that the most influential process parameter contributing to the impact energy (IE) of a dissimilar Al-Cu weld joint is rotational speed (RPM). *Shi et al.* [35] looked at how water cooling affected the microstructure and mechanical properties of friction stir welded dissimilar 2A12/6061 aluminum alloys. *Khalaf et al.* [36] investigated the effect of underwater friction stir welding heat generation on the residual stress of an aluminum alloy, AA6068-T6.

The evidence from the existing literature emphasizes the impact of friction stir welding tools on material flow and heat generation, which affects grain size, microhardness, nugget zone, mechanical properties, and various defects in welded joints. Again, stepped tool pin profiles improve material characterization of the welded joint significantly. According to *Prado et al.* [37], conical shaped tools are one of the most commonly used robust tool pin profiles in FSW due to their ease of manufacture and closeness to the self-optimized shape of the tool pin profile. During FSW processing, the conical tool pin profile demonstrated its ability to withstand extremely high thermomechanical processing conditions. The current study contrasts the flat shoulder with the conventional conical pin tool and the stepped conical tool pin profile. The total heat generated by a conventional conical should be the same as that of a newly designed

stepped tool, so a mathematical model was developed to design a stepped tool pin profile. The effect of conventional conical and stepped tool profiles on the mechanical and microstructural properties of submerged friction stir welding of aluminum alloy is investigated in this study.

Methods and material

Tool design

According to the current literature, stepped pin profiles significantly increase the microstructure and mechanical characteristics of friction stir welded joints. However, a systematic approach to developing a stepwise tool for producing a good weld connection was limited. This study aimed to develop an analytical model for stepped pin profile tool design. FSW is a thermomechanical heat addition method in which heat generated by friction and plastic deformation is employed to raise the temperature of the workpiece between 70% and 80% of its melting point.

Estimation of peak temperature

While designing the FSW tool, it is desirable to consider the thermal load in terms of a combination of thermal load action on the tool. Temperature influences the mechanical properties of a workpiece and tool material. As a result, it is critical to acquire the peak temperature necessary for FSW welding circumstances before designing an FSW tool. Welding parameters such as the tool rotation speed, the welding speed, the tilt angle, the plunging force, and the tool shape influence the peak temperature during welding. Researchers [25-27] have developed a numerical model to study thermal history, material flow, and different stresses acting during FSW. The developed model is reasonably consistent with the published literature for various materials and welding conditions. Additionally, this model may identify welding conditions that will prevent the workpiece from melting during FSW. This paper considers the same dimensionless peak temperature model to estimate the peak temperature for a given welding condition.

The following assumptions are made for mathematical modelling,

1. Total heat generated by contacting surfaces of conventional conical pin tool (Q_{TCC}) should be the same as that of the total heat generated by contacting surfaces of the stepped conical pin tool (Q_{TSC})i. e $Q_{TCC} = Q_{TSC}$
2. Temperature-dependent material properties are considered at the peak temperature generated during the in-air friction stir welding procedure.
3. Partial sliding/sticking contact conditions are considered to study heat generation due to friction and plastic deformation.
4. The angle of tool inclination is not taken into account in mathematical modelling.

T^* is the Dimensionless peak temperature from the non-dimensional heat model Q^* Dimensionless heat input valid for a range of Q^* between $5 \times 10^3$to 5×10^5,

$$T^* = 0.131\, log(Q^*) + 0.196 \qquad 1$$

$$T^* = \frac{T_P - T_{in}}{T_s - T_{in}} \qquad 2$$

$$Q^* = \frac{f\sigma_8 A\,\omega C_P}{kU^2} \quad 3$$

where T_P, T_{in}, and T_S are the peak, initial and solidus temperatures of the workpiece, respectively,

f represents the fraction of heat transported into the workpiece, σ_8 is the yield strength value at a temperature that is 80% the solidus temperature and A is the surface area of the shoulder. The thermal properties at the mean temperature defined as $\frac{T_S+T_{in}}{2}$ are used in the calculations. For the optimum process parameters and conventional conical tool geometry parameters, the peak temperature recorded is about 80% of the solidus temperature of the workpiece material. Also, Peak temperatures estimated using the above model and validated using a numerical model established by *Nandan et al.* [27] for 6061 -T6 reveals a maximum variance of 7%. As a result, a model was used to estimate the peak temperature to model the heat generation model and the tool durability index of the FSW tool.

Contact condition

The accuracy of the model is determined by the contact state conditions of sliding and sticking states during mathematical modeling. *Schmidt et al.* [38] proposed three contact state conditions for friction stir welding to develop a more accurate mathematical model: sliding, sticking, and partial sliding/sticking contact states. A sticking condition occurs when the friction shear stress exceeds the underlying matrix yield shear stress, causing the material matrix surface to twig to the moving tool's contact surface.

A sliding condition is applied when friction shear stress is less than the underlying matrix yield shear stress. The material matrix surface will slide to a stationary elastic deformation. The partial sliding/sticking contact state is considered when the friction shear stress is the same as the underlying matrix yield shear stress. This contact state promotes heat generation by friction and plastic deformation. The contact state variable δ defined by *Schmidt et al.* [38] is as follows,

$$\delta = \frac{\omega_{workpiece}}{\omega_{tool}} \quad 4$$

where $\omega_{workpiece}$ is the angular velocity of the contact matrix layer and ω_{tool} is the angular velocity of the tool. In the above equation, when $\delta = 1$, the sticking contact state, $\delta = 0$, sliding contact state, and for $0 < \delta > 1$, is a partial sliding/ sticking contact state.

In the same context, *Arora et al.* [39] proposed a new equation developed from the previous literature based on data of accumulated slip during cross-wedge rolling. According to *Arora et al.* [39], δ as a spatially variable fractional slip,

$$\delta = 0.31 \times exp\left(\frac{\omega r}{1.87}\right) - 0.026 \quad 5$$

And the coefficient of friction μ_f, between the tool and the workpiece

$$\mu_f = 0.5 \times exp\,(-\omega r \times \delta) \quad 6$$

where ωr is in m/s. Equations 5 and 6 are valid for ωr from 0.1 to 1.6 m/s. ω is the angular velocity of the tool, and r is the radial distance from the tool axis.

Heat generation model

All the surfaces of the tool pin and tool shoulder surface that interact with workpiece material generate heat due to friction and plastic deformation and are considered the heat sources are shown in Figure 2. Total heat generated by tool pin interaction in friction stir welding is calculated as follows [40].

$$Q = \oint_A \{(1-\delta)\tau + \delta\mu_f P_N\}\omega r_A dA \qquad 7$$

Where τ is the shear yield strength of the material at the specific temperature, P_N is the contact pressure between tool and workpiece, r_A is the distance of the infinitesimal small area dA at the tool axis.

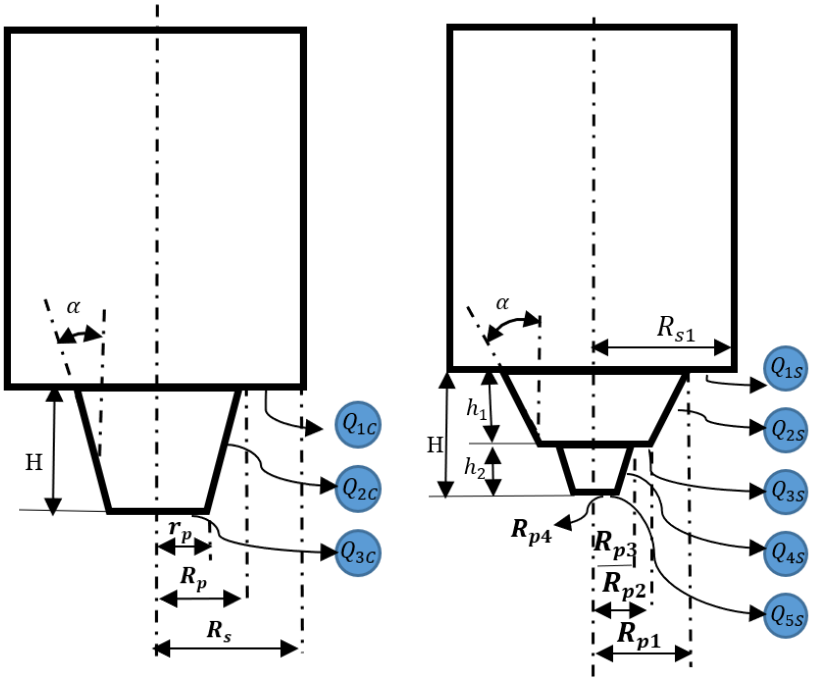

(a) *(b)*

Fig. 2. Proposed FSW tools a) Conventional conical pin tool b) Stepped conical pin tool.

In this equation factor, $(1-\delta)\tau$ denotes the heat due to the sticking, and $\delta\mu_f P_N$ factor contributes heat due to friction because of contacting surfaces of tool and workpiece. A conventional conical tool consists of three heat sources: the shoulder (Q_{1C}), pin side surface (Q_{2C}.), and pin bottom surface (Q_{3C}). The total heat generated by these regions is defined by following equations [41].

$$Q_{Total} = \left[(1-\delta)Q_{sticking} + \delta Q_{sliding}\right] \qquad 8$$

In the above equation, $Q_{sticking}$ is the heat generated by plastic deformation, and $Q_{sliding}$ is the heat generated due to frictional heating between the tool and the workpiece. Total heat generated by all contacting surfaces of the conventional tool by considering partial sticking and sliding conditions is as follows,

$$Q_{TCC} = Q_{1C} + Q_{2C} + Q_{3C} \quad 9$$

$$Q_{TCC} = (1-\delta)\omega \int_{R_p}^{R_S} \tau_b \times 2\pi r^2 dr + \delta\omega \int_{R_P}^{R_S} \mu P \times 2\pi r^2 dr + (1 -$$

$$\delta)\omega \int_0^H \tau_b \times 2\pi (r_p + htan\alpha)^{\,2} dh + \delta\omega \int_0^H \mu P \times 2\pi \left(r_p + htan\alpha\right)^2 \left(\frac{dh}{cos\alpha}\right) + (1 -$$

$$\delta)\omega \int_0^{r_p} \tau_b \times 2\pi r^2 dr + \delta\omega \int_0^{r_p} \mu P \times 2\pi r^2 dr \quad 10$$

$$Q_{TCC} = \frac{2}{3}\pi\omega[(1-\delta)\tau_b + \delta\mu P]\left(R_S^3 - R_p^3\right) + \frac{2}{3}\frac{(1-\delta)\pi\omega\tau_b}{tan\alpha}\left(R_p^3 - r_p^3\right) +$$

$$\frac{2}{3}\frac{\delta\pi\mu P\omega}{sin\alpha}\left(R_p^3 - r_p^3\right) + [(1-\delta)\tau_b + \delta\mu P]\frac{2}{3}\pi\omega r_p^3 \quad 11$$

Eq.10 is the total heat generation of the conventional conical tool in kW. By substituting

$R_S = \frac{R_p}{3}$,$r_p = R_p - htan\alpha$, δ, μ from eq. 5 and 6 and taking $\tau_b = \frac{\sigma}{\sqrt{3}}$, considering temperature-dependent material properties [42].

For the stepped conical tool profile, a more significant number of surfaces contribute to heat generation due to friction and plastic deformation shown in Figure 1. A stepped tool consisting of five heat sources shows the shoulder region (Q_{1S}), the large pin side surface Q_{2S}, large pin bottom surface Q_{3S}, the small pin side surface Q_{4S} and small pin bottom surface Q_{5S} in Figure 2.

Total heat generated by all five contacting surfaces of the stepped conical tool by considering partial sticking and sliding conditions is

$$Q_{TSC} = Q_{1S} + Q_{2S} + Q_{3S} + Q_{4S} + Q_{5S} \quad 12$$

$$Q_{TSC} = (1-\delta)\omega \int_{R_{p1}}^{R_{S1}} \tau_b \times 2\pi r^2 dr + \delta\omega \int_{R_{P1}}^{R_{S1}} \mu P \times 2\pi r^2 dr + (1 -$$

$$\delta_s)\omega \int_0^{h_1} \tau_b \times 2\pi\left(R_{p2} + htan\alpha\right)^2 dh + \delta\omega \int_0^{h_1} \mu_s P \times 2\pi\left(R_{p2} + htan\alpha\right)^2 \left(\frac{dh}{cos\alpha}\right) +$$

$$(1-\delta_s)\omega \int_{R_{p3}}^{R_{p2}} \tau_b \times 2\pi r^2 dr + \delta_s\omega \int_{R_{P1}}^{R_{S1}} \mu_s P \times 2\pi r^2 dr + (1-\delta_s)\omega \int_0^{h_2} \tau_b \times$$

$$2\pi\left(R_{p4} + htan\alpha\right)^2 dh + \delta\omega \int_0^{h_2} \mu_s P \times 2\pi\left(R_{p4} + htan\alpha\right)^2 \left(\frac{dh}{cos\alpha}\right) + (1 -$$

$$\delta_S)\omega \int_0^{R_{p4}} \tau_b \times 2\pi r^2 dr + \delta_s\omega \int_0^{R_{p4}} \mu_s P \times 2\pi r^2 dr \quad 13$$

$$Q_{TSC} = [(1-\delta_s)\tau_b + \delta\mu_s P]\frac{2}{3}\pi\omega\left(R_{s1}^3 - R_{p1}^3\right) + \frac{2}{3}\frac{(1-\delta_s)\pi\omega\tau_b}{tan\alpha}\left(R_{p1}^3 - R_{p2}^3\right) +$$

$$\frac{2}{3}\frac{\delta\pi\mu_s P\omega}{sin\alpha}\left(R_{p1}^3 - R_{p2}^3\right) + [(1-\delta_s)\tau_b + \delta\mu_s P]\frac{2}{3}\pi\omega\left(R_{p2}^3 - R_{p3}^3\right) + \frac{2}{3}\frac{(1-\delta_s)\pi\omega\tau_b}{tan\alpha}\left(R_{p3}^3 -\right.$$

$$\left.R_{p4}^3\right) + \frac{2}{3}\frac{\delta_s\pi\mu_s P\omega}{sin\alpha}\left(R_{p3}^3 - R_{p4}^3\right) + [(1-\delta_s)\tau_b + \delta\mu_s P]\frac{2}{3}\pi\omega R_{p4}^3 \quad 14$$

By assigning a geometrical relationship among the various tool design parameters of a stepped conical tool, the dimensions of the stepped tool are derived by equating the equation of total heat generation by a conventional tool and total heat generation by the proposed stepped tool, shown by combining eq. 11 and eq. 14.

Stepped conical tool dimensions were calculated by comparing the equation for total heat generation by a conventional tool and the equation for total heat generation by the proposed stepped tool, shown by eq. 10 and eq. 13.

$$Q_{TCC} = Q_{TSC}$$

By finding a geometrical relationship among stepped tool dimensions, the equation total heat generation by the stepped conical tool (Q_{TSC}) was reduced to R_{S1}, α, and H geometrical parameters of the stepped tool. The equation for total heat generation by a stepped conical tool (Q_{TSC}) was reduced to $the\ stepped\ tool's\ R_{S1}$, α, and H geometrical parameters by discovering a geometrical relationship among stepped tool dimensions. $R_{p1} = \frac{R_{S1}}{n}$ (n=D/d ratio- 2, 2.5, 3, 3.5), $R_{p2} = R_{p1} - h_1 tan\alpha$, $R_{p3} = \frac{R_{p2}}{n}$, $R_{p4} = R_{p3} - h_2 tan\alpha, h_1 = h_2, H = h_1 + h_2, \alpha = 14°$ (for the conical tool and a stepped tool).

Geometric parameters of the tools calculated using a Microsoft Excel tool. The path followed to do the analysis: MS Excel-Data-What-If Analysis- Goal seek analysis. To analyse the effect of tool diameter ratio on mechanical and microstructural analysis of FSW joint different D/d ratios $=\frac{R_{S1}}{R_{p1}}=\frac{R_{p2}}{R_{p3}}$ for each tool were considered, varying between 2 to 3.5. Table 1 shows the tool pin parameters with equating equations of total heat generation of conventional tool and proposed stepped tool modelled analytically. Figure 3 (a) and (b) shows solid modelling and actual manufactured stepped tools using the CNC machining process for a given dimension with different D/d ratios.

Table 1. Tool dimension with tool durability index.

Tool type	**Tool Dimensions (in mm)**								**τ_{max} (MPa)**	**Durability (I)**
TCT.	**Conical tool**		**$R_s = 9$**	**$R_p = 3$**	**$r_p = 1.6$**	**$H = 5.6$**			**38.04**	**14.46**
			R_{s1}	R_{p1}	R_{p2}	R_{p3}	R_{p4}	$h_1 = h_2$		
CST1	Stepped tools	D/d =2	9.43	4.72	4.02	1.34	0.65	2.8	52.29	10.52
CST2		D/d =2.5	9.64	3.86	3.11	1.04	0.31	2.8	84.62	6.50
CST3		D/d =3	9.74	3.25	2.55	0.85	0.16	2.8	149.42	3.68
CST4		D/d =3.5	9.80	2.80	2.13	0.71	0.2	2.8	258.95	2.12

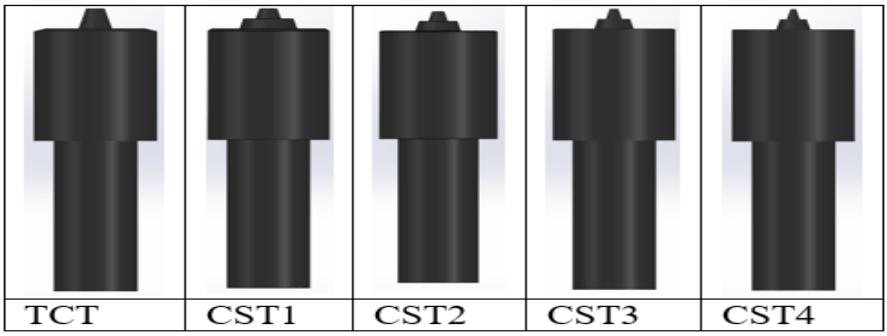

(a)

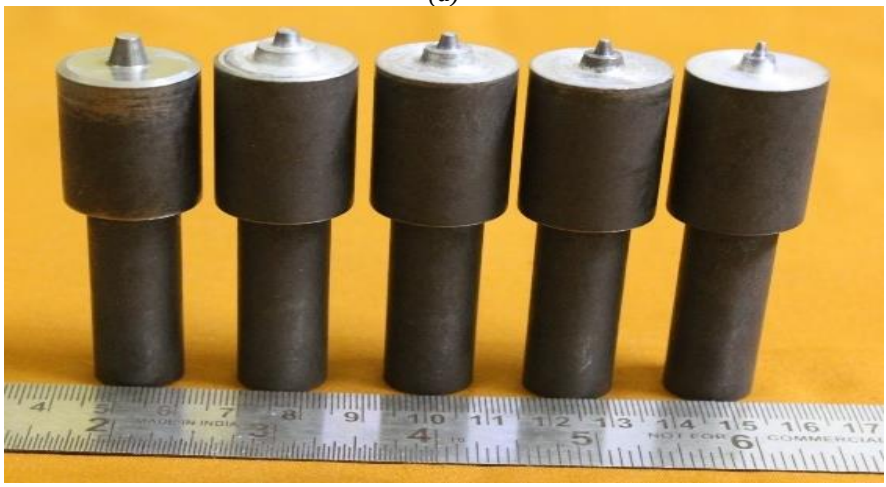

(b)

Fig. 3. Stepped Tools: a) Solid modelling b) Actual machined tools.

Tool durability index (I)

The FSW tool plays a crucial role in heat generation and plasticized material during FSW. FSW tool undergoes combined torsion and bending due to simultaneous rotational and translational movement in the workpiece. The pin is subjected to fluctuating stresses because of the combined torsion and bending stresses. Resultant stresses and high temperatures lead to failure of the pin during welding of harder materials increased resulting stresses beyond tool bearing capacity led to wear and premature loss of the tool. Mechanical erosion, chemical erosion due to the interaction between tool and workpiece material, and fatigue and fracture limit friction stir welding tool , as the pin is the weakest member of the FSW [43]. The selection of tool geometry and its dimension plays a significant role.

Due to the simultaneous translational and rotational motions of the plasticized workpiece material, the tool pin experiences combined bending and torsion during FSW. Estimating the forces acting on the tool pin is difficult because it is submerged in the workpiece. Because of the linear motion of the FSW tool, the tool pin will feel normal force in the opposite direction of welding (welding speed). The force would be greater towards the bottom of the pin because the material farthest from the tool shoulder is colder and stronger. In FSW, the pin inside the workpiece experiences normal force rather than welding force as the tool travels through the workpiece at welding speed. During welding, the top of the workpiece is exposed to air, and the bottom region is in contact with the fixture. As a result, the top surface loses heat due to natural convection, while the bottom has a relatively high conduction mode. The temperature at the top of this workpiece, near the shoulder region, is very hot, while it is relatively cold at the bottom; this results in more forger at the bottom of the pin when compared to other areas. Figure 4 depicts a schematic representation of a typical force distribution, q (z), on a straight cylindrical FSW tool pin (a). The force distribution, q(z), acts on the tool pin in the opposite direction to the welding direction due to the yield strength of the welding material at the respective welding temperature.

A transverse cross-section of the tool pin along S–S in is shown in Figure 4 (b). where H is the length of the pin, z1 is the distance of the point A from the root of the pin, q(z)is the force on the infinitesimal part of the pin dz at (z+z1) distance from the root of the pin. For a tapered pin, a radius of the cross-section at a distance x from the pin bottom is calculated using a pin which R = Radius of large c/s of a pin, r= Radius of smaller c/s of a pin.

$$r(x) = r + \left(\frac{(R-r}{h}\right) * x$$

Figure 4 (a) shows a cross-section FSW tool along the transverse direction to the horizontal plane. Figure 4 (b) shows a cross-section of the pin profile along the horizontal plane at lines S–S, where L is the length of the pin, z1 is the distance of point A from the root of the pin, q(z)is the force on the infinitesimal part of the pin dz at (z+z1) distance from the root of the pin.

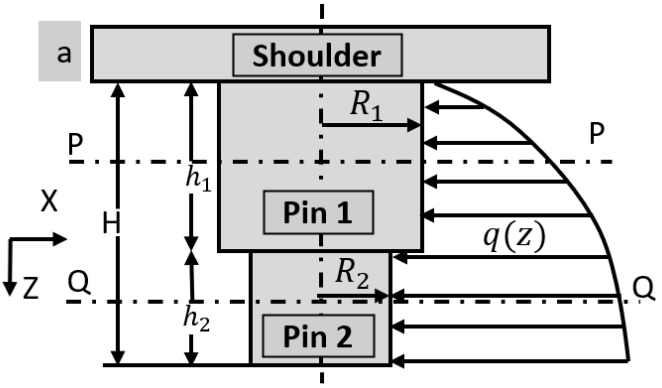

(a)

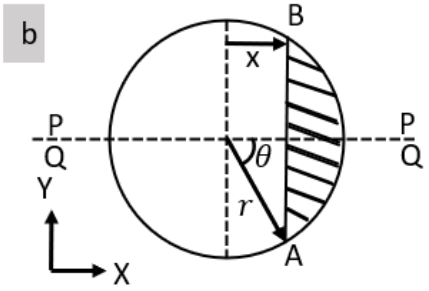

(b)

Fig. 4. (a) Schematic of a friction stir welding tool (b) Cross-section at S-S.

A spindle motor transmits the power to the tool at a specified rotational speed. During the interaction between tool and workpiece, resisting torque M, acting on the tool is the sum of its components sliding torque M_L and Sticking Torque M_T, $M_L + M_T$, estimates as,

$$M_L = \int_{R_{P1}}^{R_{S1}} \delta_S \mu P \times 2\pi r^2 dr + \int_0^{h_1} \delta \mu_s P \times 2\pi \left(R_{p2} + htan\alpha\right)^2 \left(\frac{dh}{cos\alpha}\right) +$$

$$\int_{R_{P1}}^{R_{S1}} \delta_s \mu_s P \times 2\pi r^2 dr + \int_0^{h_2} \delta_s \mu_s P \times 2\pi \left(R_{p4} + htan\alpha\right)^2 \left(\frac{dh}{cos\alpha}\right) + \int_0^{R_{p4}} \delta_s \mu_s P \times$$

$$2\pi r^2 dr$$

$$M_T = (1-\delta_s)\int_{R_{p1}}^{R_{S1}} \tau_b \times 2\pi r^2 dr + (1-\delta_s)\int_0^{h_1} \tau_b \times 2\pi\left(R_{p2} + htan\alpha\right)^2 dh +$$

$$(1-\delta_s)\int_{R_{p3}}^{R_{p2}} \tau_b \times 2\pi r^2 dr + (1-\delta_s)\int_0^{h_2} \tau_b \times 2\pi\left(R_{p4} + htan\alpha\right)^2 dh +$$

$$(1-\delta_S)\omega\int_0^{R_{p4}} \tau_b \times 2\pi r^2 dr$$

As the tool traversed along the welding line with specified RPM and welding speed, the tool experienced resistive force F in the form of frictional tractive force F_s under the action of vertical plunge force/Pressure acted upon the shoulder, and the pin experienced resisting force due to yield strength of workpiece material. Tool traverse force $F = F_S + F_P$, can be estimated as

$$F_S = \int_{R_P}^{R_S} \delta\mu_f P_N \times (2\pi r\, dr)$$

$$F_P = \int_0^L \sigma_y \times dA$$

The normal stress due to bending, σ_B, is calculated as [23, 43-45]:

$$\sigma_B = \frac{4\cos\theta}{\pi r^3}\int_{z1}^{H} zq(z)\, dz$$

The shear stress, τ_T, at point, A due to torsion can be calculated as [43-45].

$$\tau_T = \frac{2\, M_T\, r}{\pi r^4/2}$$

The shear stress, τ_B, at point, A due to bending can be computed as [43-45].

$$\tau_B = \frac{4}{3}\frac{\cos^2\theta}{\pi r^2}\int_{z1}^{H} q(z)\, dz$$

Following Tresca's criterion, the maximum shear stress, τ_{max},on the tool pin is obtained by considering σ_BBending stress, τ_B shear stress due to bending, and τ_T due to torsion is [43-45].

$$\tau_{max} = \sqrt{\left(\frac{\sigma_B}{2}\right)^2 + (\tau_B + \tau_T sin\theta)^2 + (\tau_T\, cos\theta)^2}$$

The stresses on the tool pin are estimated using these equations. The pin is the weakest member of the FSW tool due to high fluctuating stresses. As a result, the highest stresses acting on the tool rather than the tool pin are regarded as these stresses. To calculate the durability index, *Arora et al.* [39] used temperature-dependent material properties to consider shear yield strength for each tool's respective peak temperature during the process. The tool durability index (I) is the ratio of the shear yield strength of the tool material to the maximum shear stress experienced by the tool pin. Table 2 displays the durability indices of conical and stepped tools with varying D/d ratios.

Table 2. Tool durability index

Type	Nomenclature	D/d Ratio	τ_{max} (MPa)	Durability (*I*)
Taper conical tool	TCT	2	38.04	14.46
Conical stepped tools	CST1	2	52.29	10.52
	CST2	2.5	84.62	6.50
	CST3	3	149.42	3.68
	CST4	3.5	258.95	2.12

Experimental details

In this research, rolled plates of aluminum alloy AA 6061-T6 of 6 mm thickness are considered for the experimentations. Table 3 and Table 4 show the chemical composition and mechanical properties of AA 6061-T6 respectively. Aluminum alloy sheets were cut into a sample size of 200 (L) x 75 (W) x 6 (T) mm and were considered for the welding cut from the Aluminum alloy sheets with abrasive cutting and rough cutting edges machined with the Milling machine. Edge of 200 mm length was considered along welding path, cut so that the rolling direction of base plate should be perpendicular welding line. All the welding specimens were washed with acetone to avoid any contamination from foreign sources. The conical tool and the stepped conical pin tool profile were selected for the welding procedure. Tools were machined from 22 mm dia. Hot worked die steel (AISI- H13) and hardened up 50-55 HRC before machining to avoid any variation in the tool dimensions. The chemical composition of H13 Hot worked die steel (AISI- H13) C-0.4, Mn-0.4, Si-1, Mo-1.35, Cr-0.25, V-1, and Fe-balance (all elements in wt.%) was tested with optical emission spectroscopy.

Table 3. Chemical composition of AA6061-T6 alloy

Elements	Mg	Si	Mn	Zn	Fe	Cu	Al
Alloying elements (%)	1.1	0.6	0.12	0.25	0.35	0.3	Rest

Table 4. Mechanical properties of AA6061-T6 alloy

Properties	Ultimate tensile strength, MPa	Tensile yield strength, MPa	Modulus of elasticity, GPa	Percentage elongation, %	Poisson's ratio	Melting point temp. in °C	Hardness, Vickers (Hv)	Density (g/cc)
Values	303	240	68.9	20	0.33	582-652	107	2.7

The experiments in Figure 5 were carried out on a universal milling machine (G. DUFOUR make 624D model) equipped with a vertical spindle tilt attachment and a DRO. The milling machine has a 15 HP main spindle motor with a spindle speed range of 24-1180 rpm. There are also two feed motors with 5 HP power and a speed range of 22-1180 mm/min. Figure 5 depicts the underwater FSW experimental setup. FSW tool mounted with collet on universal milling machine spindle. The fixture was securely fastened to the

milling machine's bed. Figure 6 depicts a special-purpose enclosed fixture designed for welding trials that can properly hold the workpiece and withstand the load acting on it when exposed to water.

Fig. 5. Experimental setup.

Specimens were rigidly clamped to restrict lateral and transverse movement of the specimen during trials to make a defect-free joint. Firstly, the rotating tool shoulder is allowed to touch the specimen's top surface, and then water is allowed to pour into the fixture vessel to make a 20 mm water head.

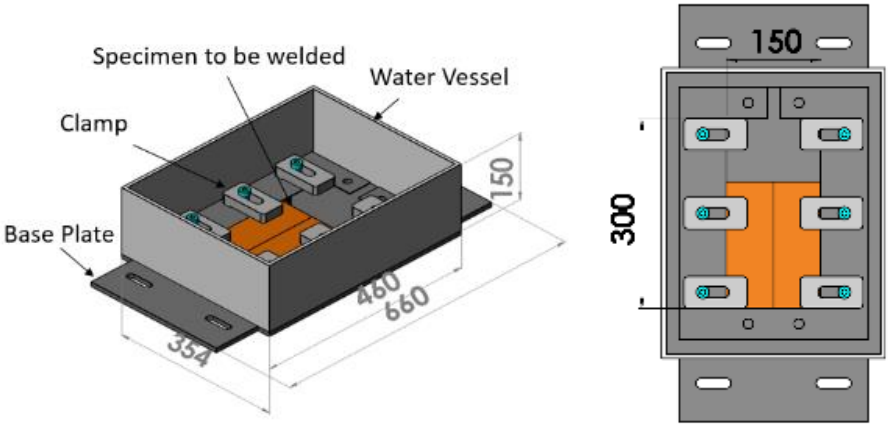

(a) Isometric view *(b) Top view*

Fig. 6. Underwater friction stir welding fixture a) Isometric view b) Top view.

The main parameters that affect the mechanical and microstructural properties of the welded joint in friction stir welding are tool geometry, tool dimensions, tool material, tool rotation speed, welding speed, tilt angle, plunge depth, axial load, and submerged conditions. The welding trials in this study were conducted using the parameters shown in Table 5. Welded samples were cut into tensile test specimens using Abrasive water jet

cutting in accordance with American Society for Testing of Materials (ASTM) E-8M-08 [ASTM-2008] guidelines. Tensile tests were carried out on a universal testing machine (UTM) with a capacity of 2000KN (Make: Universal Motion Inc, Model: MUTCS-20 model) and a crosshead speed of 1 mm/min.

Table 5. Process parameters and their values.

Parameter (Notation)	Unit	Value
Tool rotation speed (TRS)	RPM	900
Welding speed (WS)	mm/min	108
Tilt angle (TA)	° degrees	2°

Macro and microstructure evaluation using a light optical microscope (Make: Conation technologies) with an image analyzing system has been conducted with optical microscopy. All the microstructure samples were polished to different grades of emery paper followed by a diamond paste of 1 μm particle size to evolve different zone of welded specimen SZ, TMAZ, HAZ, and base material. EBSD analysis was performed using Oxford CMOS-based EBSD detector to study grain size in the nugget zone due to limitations in the optical microscope to identify the grain size. The electropolishing by a solution of 10% perchloric acid in ethanol and Keller's reagent was applied for EBSD analysis. It is challenging to distinguish the grain boundaries of Aluminum alloys in welds using optical metallography. More recently, new etchants have been discovered that make it simpler to use an optical microscope to examine AA 6061-T6 welds. But at magnifications lower than a grain, optical metallography is unable to offer a sufficient level of resolution. Therefore, it is crucial to examine the grain boundary and its orientation for AA 6061-T6. Since considerable plastic deformation is known to occur during FSW, texture and microstructure will be produced during the process. The process of microstructure and texture evolution during FSW is still not well understood since the stress state, material flow, and temperature history are all rather complex. An EBSD map is more useful thoroughly in order to examine the microstructure and macrotexture of FSW joints. Microhardness testing was carried on in the mid of the weld zone (transverse to weld direction). It was considered a testing area with a 1 mm interval using 100g indentation load for a dwell time of 15 second with Vickers microhardness tester of (Econo met make) VH-1MD.

Result and discussions

Tool durability index

The durability index assesses a material's capacity to endure a load during manufacturing. The stepped geometry tools are obtained using a mathematical model created in this study. Their tool durability index was calculated using the principle of mechanics by considering combined bending and the torsion load on the tool pin with temperature-dependent material properties. It is desirable to have an optimum tool durability index because as the index rises, tools become safer, but material costs and tool processing costs rise, and vice versa. During welding, if the maximum shear stress is greater than the tool material's shear yield strength at peak temperature, the tool will fail prematurely [42, 46].

Figure 7 depicts the tool durability index for conical and stepped profile tools with various D/d ratios ranging from 2-3.5 in the interval of 0.5 and the same process parameters. The graph referred to by *Debroy et al.* [43] is used to calculate the shear strength of H13 at welding peak temperature. The maximum shear stress measured with the traditional conical tool is 34.5 MPa, which falls within the 29-65 MPa range estimated by *Arora et al.* [39] for FSW of Base material 6061-T6. The durability index of a stepped tool decreases as the tool D/d ratio increases. As the D/d ratio increases, the pin diameter decreases, putting more strain on the tool pin and increasing its maximum shear stress. According to *Arora et al.* [39], a larger diameter tool pin can handle more bending and torsion moments while maintaining the same pin length.

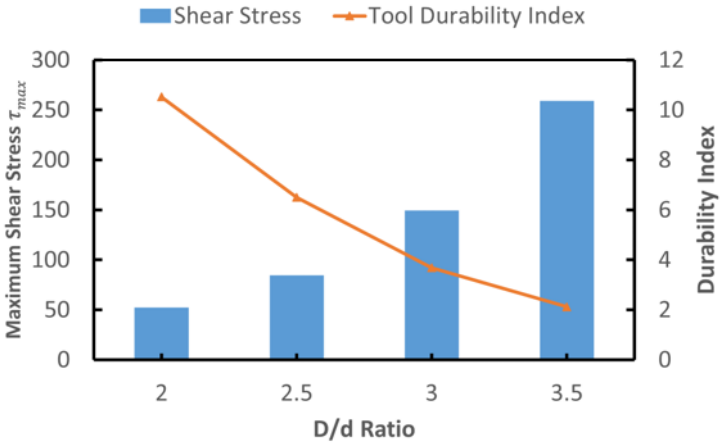

Fig. 7. Effect of D/d ratio on Maximum shear stress and Tool durability Index.

Furthermore, the author discovered that increasing the shoulder diameter raises the peak temperature while decreasing the forces acting on the pin and the maximum shear stress. In this study, the variation in shoulder diameter is not as dramatic as the variation in shoulder diameter observed by *Arora et al.* when the D/d ratio increases. As a result, stepped tools with D/d ranging from 2 to 3.5 increase tool diameters while lowering the tool durability index.

Microscopic analysis

Figure 8 shows macrographs of welded specimens with different tool pin profiles used in this study. The micrographs all show four distinct zones that are commonly found in the macrostructure of FSW joints. A friction stir welded joint's macrograph is frequently divided into four areas: the stir zone (SZ), the thermo-mechanical affected zone (TMAZ), the heat-affected zone (HAZ), and the base metal (BM). There are no flaws in either macrograph, indicating that the welding process parameters were correctly specified for the tool geometry comparison.

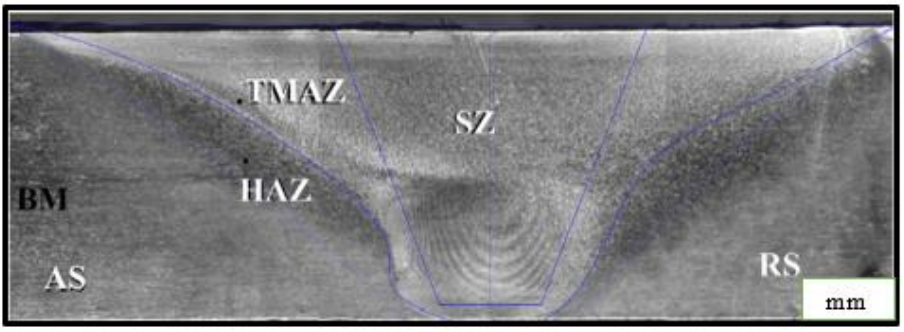
TMAZ
SZ
BM
HAZ
AS
RS
mm

(a)

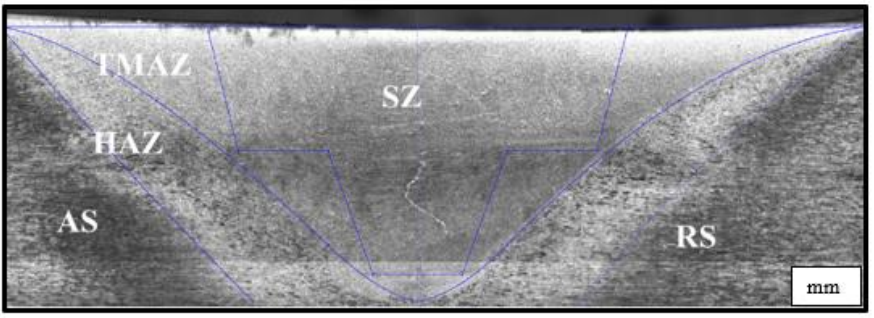
TMAZ
SZ
HAZ
AS
RS
mm

(b)

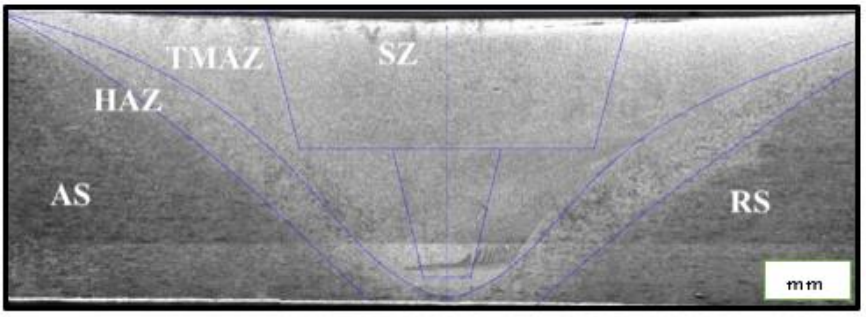
TMAZ
SZ
HAZ
AS
RS
mm

(c)

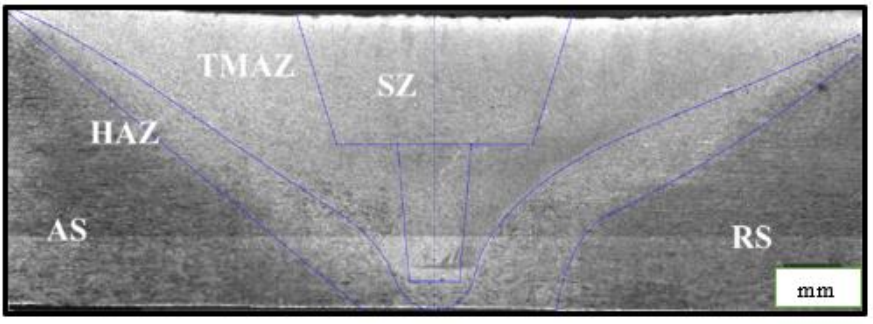
TMAZ
SZ
HAZ
AS
RS
mm

(d)

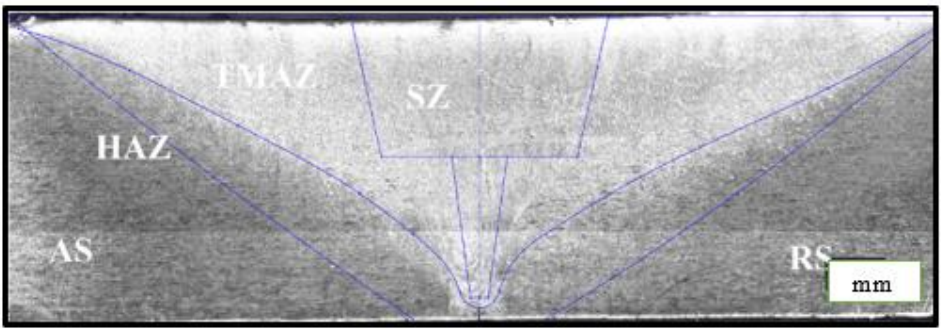

(e)

Fig. 8. Macrostructure of friction welded specimen by (a) TCT (b) CST 1 (c) CST 2 (d) CST 3 (e) CST 4.

TMAZ zone of stepped conical tool pin profile is wider than its counterpart shown in Figure 8, stir zone of the conical tool shows a distinct onion ring pattern compared to very small onion rings at the bottom of stepped pin profile. *Kumar et al.* [7] observed that due to the interaction of pin driven flow with shoulder and upright movement of material due to shoulder. Layered pin-driven flow and bulk shoulder-driven flow are responsible for joint formation.

Shoulder-driven flow is significant in FSW samples welded with stepped tools due to its large diameter, which suppresses the effect of layered pin-driven flow and reduces the formation of the onion ring profile in the nugget zone. When compared to the conical tool, increase the shoulder diameter in steps to increase the size of the nugget zone and TMAZ. A step in the middle of the heat-affected zone indicates that the step on the tool pin contributes to heat and plastic deformation. In stepped pin profile tools, each step acts as the shoulder for the next bottom pin, contributing heat due to friction and plastic deformation, resulting in uniform heat distribution and grain refinement. According to Chandran and Santhanam [47], typical friction welding at rotating speeds of 800 and 1200 rpm produces the best weld shape, free of flaws, due to proper heat generation of the welded material. The bottom of the stir zone narrows as the tool pin diameter ratio increases from 2 to 3.5, as shown in Figure 8.

Since grain size analysis has a significant impact on the mechanical properties of the welded joint. This research looks at the variation in grain size before and after friction stir welding in different regions of the weld nugget zone, as well as its tensile properties and fracture analysis. Grain refinement occurs in FSW as a result of intense recrystallization caused by stir action, which is responsible for changing mechanical properties in a welded joint. Underwater friction stir welding, once again, reduces the thermal exposure nugget zone, which restricts grain growth due to natural aging during the cooling of the joint, which adds an extra benefit to improve the mechanical properties of the joint. According to the Hall-Petch equation, as grain size increases, so does the microhardness and tensile strength of welded joints [50].

Grain subdivision at the cooler perimeter of the tool's deformation zone, as well as the geometric effects of strain, drive the grain refining process, which reduces the overall high angle border spacing with increasing deformation. Nonetheless, it involves thermally induced high-angle grain boundary migration, which becomes more pronounced as the

temperature approaches the tool. The nugget grain structure becomes more equiaxed and slightly coarsens as a result of static annealing in the thermal wake of the tool. As previously stated, discontinuous recrystallization occurs at sites with relatively large deformation stresses; however, continuous recrystallization is also accompanied by grain refining. According to studies of misorientation distribution in the literature, a steady change from low-angle borders to high-angle borders can be detected in the SZ.

The FSW process's plastic deformation severely compresses the pre-deformed coarse grains, resulting in the formation of extremely fine recrystallized equiaxed grains within the weld nugget. Furthermore, the dynamic recrystallisation (DRX) phenomenon, which is thought to be caused by dislocation adsorption at sub grain boundaries, may have aided in the nucleation and development of ultrafine grains in the FSW weld nugget.

As grain refinement occurs, which leads to an increase in microhardness, the tensile strength of the joint increases due to water acting as a cooling medium, rapidly removing heat from the weld specimens. Because of the rapid cooling, grain growth is restricted, resulting in refined grains in the weld nugget zone. The slight variation in grain size of FSW welded samples from both tools demonstrates that the cooling effect of water dominates the development of tool pin profiles with the same process parameters. EBSD techniques are also used to analyze the microstructure of all specimens welded with conical and stepped tools. The EBSD maps are shown in Figure 9 (a), and the microstructure of the base metal (AA 6061-T6) is shown in Figure 9 (b), which shows elongated grains with an average grain size of 80 m. Figure 10 depicts the components and grains map of the TMAZ prepared by taper conical tool (TCT), where taper conical tool specimens show refined grains with an average size of 7.12 m in the TMAZ zone. TCT prepared the TMAZ boundary map. In the TMAZ zone of the conical stepped tool 1 (CST1), as shown in Figure 11 (a), slightly more refined grains of size 4.9 m were observed when compared to the TCT. In comparison to the conventional TCT, the CST1 produces refined grains. Steps in the conical stepped tool refine grains in the welding zone, resulting in effective heat distribution and plastic deformation when compared to the taper conical tool.

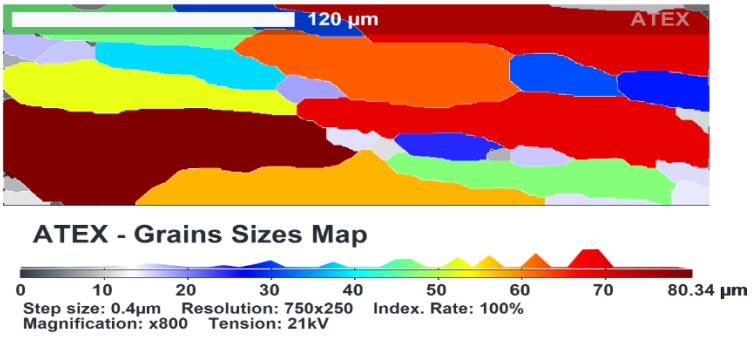

(a)

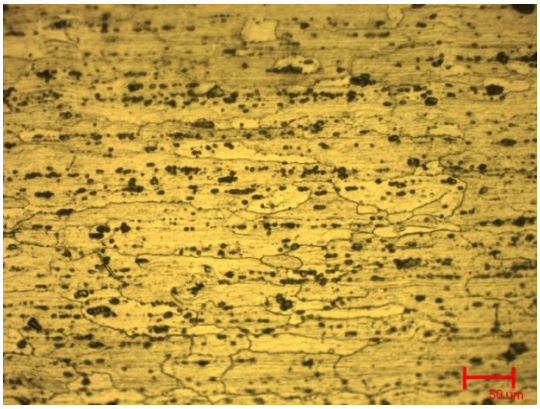

(b)

Fig. 9. (a) Grain size map of base metal (b) Microstructure of base metal.

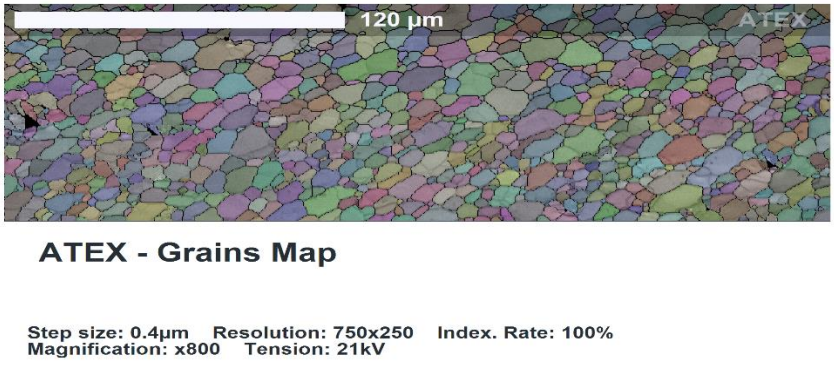

Fig. 10. Grains map of TMAZ prepared by taper conical tool TCT.

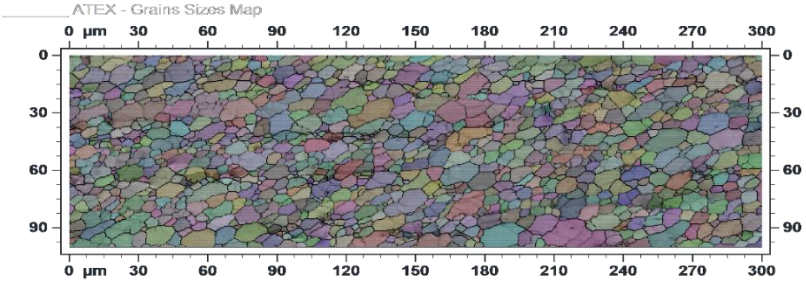

Fig. 11. Grain size map of TMAZ prepared by CST1.

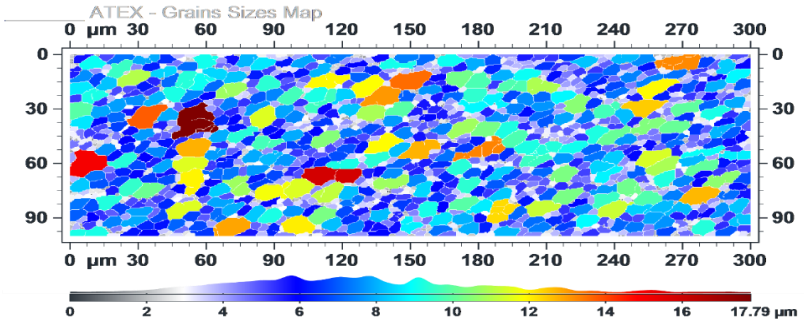

Fig. 12. Grain size map of TMAZ prepared by CST2.

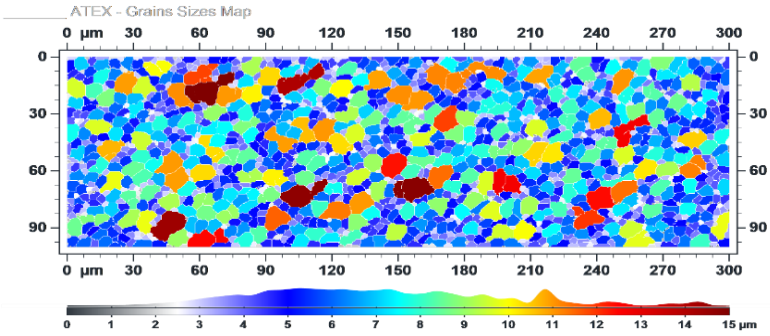

Fig. 13. Grain size map of TMAZ prepared by CST3.

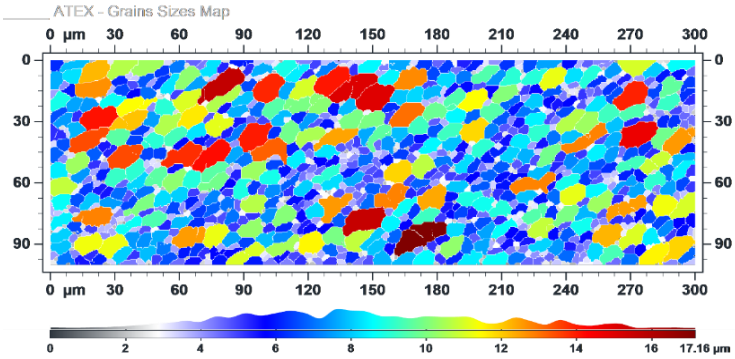

Fig. 14. Grain size map of TMAZ prepared by CST4.

Figure 12 shows a grain size map of a TMAZ prepared by the CST2 tool on both the advancing and retreating sides. Individual grains are colored on the maps based on their crystallographic orientation relative to the normal direction. The orientation code triangle indicates regions of the same crystal orientation with a distinct color. The size and shape of grains vary across the stirred zone at the TMAZ. This is due to the varying

degrees of plastic deformation and temperature rise during FSW. The fine-grained structure of the stirred zone is thought to be the result of dynamic recrystallisation during the FSW process. The TMAZ, on the other hand, has larger, elongated grains, especially on the advancing side. The grain size in the TMAZ was assessed using orientation maps. The position of the grains in relation to the weld center determines their shape. Grain is roughly equiaxed on the receding and advancing sides. This region has partially recrystallized, as evidenced by the extended grains. The crystallographic texture was precisely defined using pole figures.

Figure 13 depicts the grain size map of the TMAZ prepared by CST3. The observed average grain size of the TMAZ for this tool is 4.1 m, which is less than CST 1 and CST 2 (CST 1 =4.9 m, CST 2 =4.4 m, and CST 3 =4.1 m). The parent grains tend to be reoriented along the flow pattern around the pin due to shear deformation caused by the rotating tool, which is a TMAZ characteristic. The presence of dynamic recrystallization is indicated by the observation of newly formed equiaxed grains (DRX). More equiaxed grains are developing from the exterior to the interior of the TMAZ. Higher temperature and more locational deformation are obtained as one moves closer to the weld's core, resulting in an increase in DRX. The texture change occurs on the TMAZ border. Changes are concentrated in a small area. This region also has a wide range of grain sizes. The texture intensities on the approaching and retreating sides differ. The tested zones have different misaligned grain boundaries. The majority of the TMAZ's boundaries are at low angles.

Al alloys are common FCC alloys because they have a high stacking fault energy and are easy to recover, allowing dislocations to glide, climb, and cross slip. The Grain size map of TMAZ prepared by CST4 is shown in Figure 14, and the observed average grain size of the TMAZ is 5.12 m. The CST 4 TMAZ's twin are map and pole map, which reveal the rotated and extended deformation microstructure. Furthermore, several sub grains and a few equiaxed fine grains were observed, demonstrating that TMAZ has both dynamic recovery (DRV) and partial DRX. When compared to TCT, the TMAZ of all specimens (prepared by CST1, CST2, CST3, CST4) has significantly stronger texture when compared to the base material (Fig. 9). When compared to all tools considered, the microstructure of CST3 is refined; the number of freshly generated equiaxed grains in TMAZ on the retreating side is significantly lower than on the advancing side.

Microhardness analysis

Figure 15 (a) and (b) show microhardness maps of conical tool and stepped tool welded specimens' base material and nugget zone. Microhardness is one of the measures used to investigate the elasticity, plasticity, and strength of a welded joint. The average microhardness of the base material is 105 Hv. The microhardness analysis of samples welded with the conical and stepped tools reveals that softening occurs in the weld zone. The microhardness profiles on all of the tool samples are "W" shaped. The TMAZ zone of weld samples from both tools shows a low hardness distribution zone (LHDZ). The TMAZ zone of the stepped tool is broader as the shoulder diameter and the effect of steps on the tool increase, but the hardness value in LHDZ is higher than the conventional conical tool. The TMAZ zone of the conical tool's advancing side (AS) has a hardness value of 68 Hv, while the stepped tool has the lowest value of 71 Hv along the nugget zone's retreating side. The average microhardness in the midsection of the welding sample stepped tool is 90 Hv greater than the conical tool's 59 Hv. A rise in microhardness value

in the TMAZ zone and the entire range is attributed to slightly refined grains in TMAZ zone stepped tool samples.

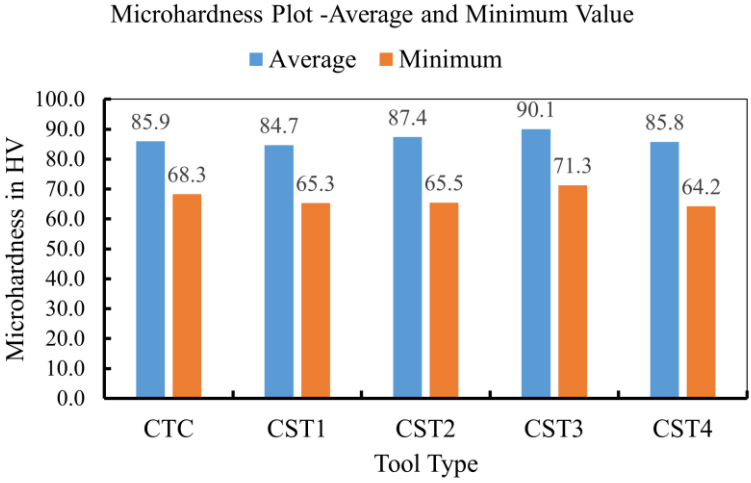

(a)

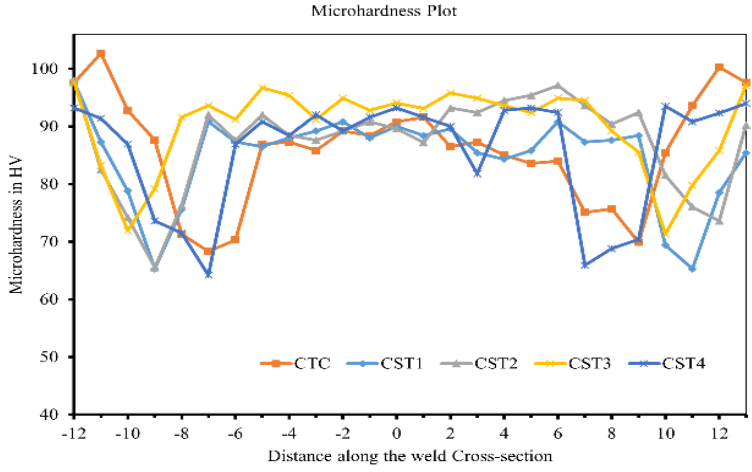

(b)

Fig. 15. (a) Microhardness plate of tool profiles (b) Average and minimum microhardness plot.

Furthermore, higher microhardness values in the stir zone confirm the severe grain refinement caused by underwater friction stir welding [48]. The stirred zone has the highest average microhardness LHDZ value of 90 Hv, while the joint fabricated by stepped tool profile CST3 and CST4 has the lowest hardness value of 64 Hv. *Salari et al.* [24] and *Prakash et al.* [49] observed a change in hardness due to high-temperature distribution and uniform material flow in the stepped-conical probe profile tool,

improving material mixing and enhancing material movement in the stirred zone. According to the results, the stepped tool CST3 with D/d ratio 3 has the best mechanical properties due to adequate heat flow, improved material mixing, and enhanced movement in the stirred zone.

Tensile test results

Figure 16 depicts tensile test plots of base material and friction stir welding specimens welded with conventional conical and stepped conical pin profile tools. Thermal cycles occur during friction stir welding, which affects mechanical characterization after welding. The tensile strength of the base material (BM.) AA 6061 T-6 is 304 MPa, the elongation is 20%, and the yield strength is 173.2MPa. Conical tool specimens have tensile strength of 237 MPa (78% of BM), elongation of 12.62%, and yield strength of 130 MPa (75% of BM). Furthermore, specimens with a stepped conical tool have tensile strength of 245 MPa (81% of BM), 75% elongation, and yield strength of 140 MPa (81% of BM). Using the stepped conical pin tool, specimens show a marginal increase in ultimate tensile strength, yield strength, and elongation. Increased material properties of welded specimens using stepped conical tool pin profile are caused by refined grains in the nugget zone and an increase in the magnitude of microhardness in the LHDZ zone. Standard tensile test specimens of FSW joint with stepped conical pin profile tool have higher tensile properties than conventional conical tool pin profile, according to the tensile test results.

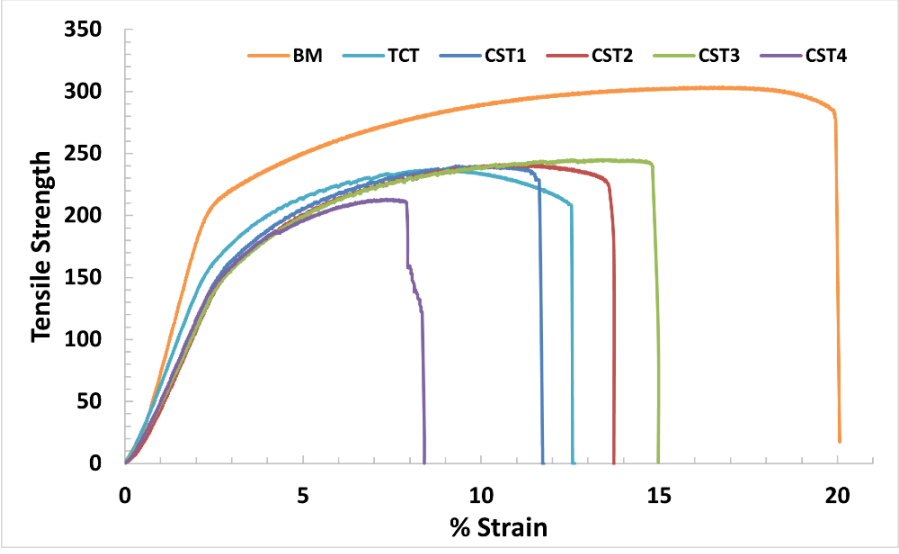

Fig. 16. Tensile strength plots of TCT and CST1, CST2, CST3, CST4 pin profile tools.

Stepped conical pin profile tools have extra surfaces that contribute to frictional heating and plastic deformation. Effective heat distribution caused by the addition of stepped heating surfaces in the nugget zone affects material flows and tends to change grain size in the nugget zone [20]. TCT, CST1, and CST2 probe profile tool joints have equivalent yield strength and ultimate tensile strength. The yield strength, ultimate tensile

strength, ductility, and joint efficiency of the CST 3 with D/d=3 weld joint are superior, while the CST4 with D/d=3.5 probe is lower. The stepped tool CST4 has a minimum joint efficiency of 70% and a maximum joint efficiency of 82% of BM.

Fracture analysis

Figure 17 depicts the fracture sites of tensile test specimens. There are two types of fracture failure regimes: crack initiation and crack propagation. The microstructure of the material has a significant influence on both regimes in the case of the current FS welded Al alloy specimen. Figures 18 (a and b) show typical SEM micrographs taken along the thickness of the FSW joint with a taper conical tool (TCT), while Figures 18 (c and d) show a stepped tool with a D/d ratio of 3 for the specimen prepared with the CST 3 tool. Figures 18 and 19 show the tensile fracture surface of a CST3 tool FSW sample with numerous dimples and second-phase particles of various shapes and sizes (c and d).

Cracks in specimens with a heterogeneous grain structure began in the layer of coarse, recrystallized grains, according to fractographic studies. Because the layer of recrystallized coarse grains is thin, the primary length of stage II crack formation may occur in both the fibrous grain structure region and the mixed grain structure region. The conical tool welded sample fails due to a crack that begins on the retreating side of the TMAZ zone, whereas the stepped tool welded specimen begins on the retreating side of the TMAZ zone, both of which are at their respective LHDZ zones. Because the crack initiation occurs at the surface layer of coarse recrystallized grains in this case, the failure is most likely due to simpler fracture initiation and stage I crack propagation. The fracture then grows in two directions: upwards at 45°, gently bending through the TMAZ and HAZ, and vertically upward in the flow arm zone. Second, the fracture began at the tool marks and spread vertically downhill from the right angle of the tunnel into the HAZ. Despite the depression at the base of the weld nugget or the TMAZ area, the specimen cracked almost along the joint line after being welded with TCT.

In this case, the fracture path approached the lowest hardness of the weld, and failure occurred at higher microhardness sites. Features such as the weld's root, tool marks, a portion of the onion ring structure, and an area of quick fracture were identified on the fracture surface towards the lower section of the weld. Weld tunnels were formed as a result of the weakened bonding between the onion structure and the weld root. Tool marks and bands of unconsolidated material were also observed. The tool mark was an incomplete semi-circular feature formed by the tool's motion on the material at the weld's root, whereas the onion ring was formed by successive material deposition, rotated and pushed down around the tool pin, but failed to be consolidated with the weld's root at the advancing side of the tool. As indicated by microhardness maps, this specimen most likely failed in the relevant zone due to softening on the retreating side of the TMAZ zone. Figure 18 (a) and (b) show intergranular cracking at the second-phase boundary as either a split between the network-like grain boundary phase and grains or a natural fracture of the grain boundary phase. Simultaneously, despite the presence of numerous second-phase particles, additional dimple-like characteristics emerged on the FSW joint's fracture surface. The ripping ridges were densely packed with micropores, indicating ductile fracture.

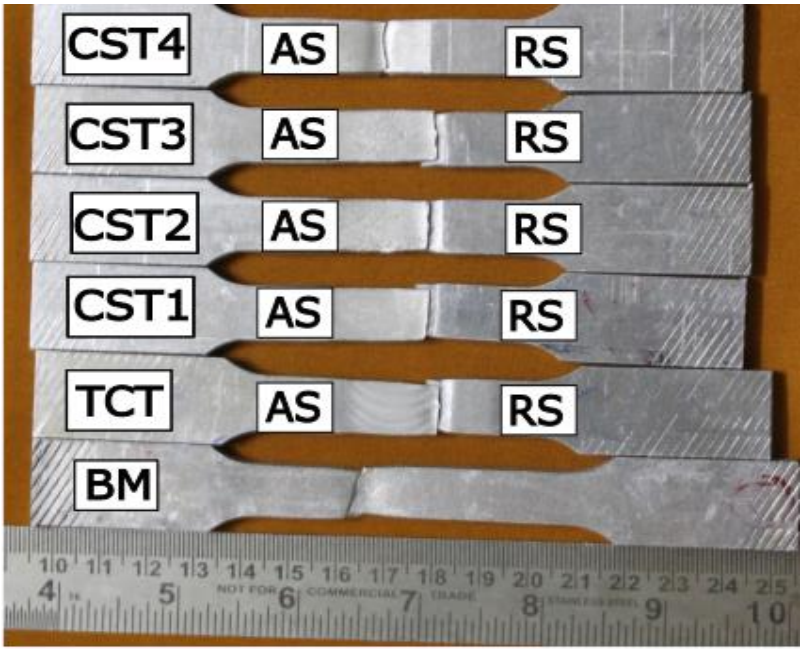

Fig. 17. Fracture locations of tensile test specimens.

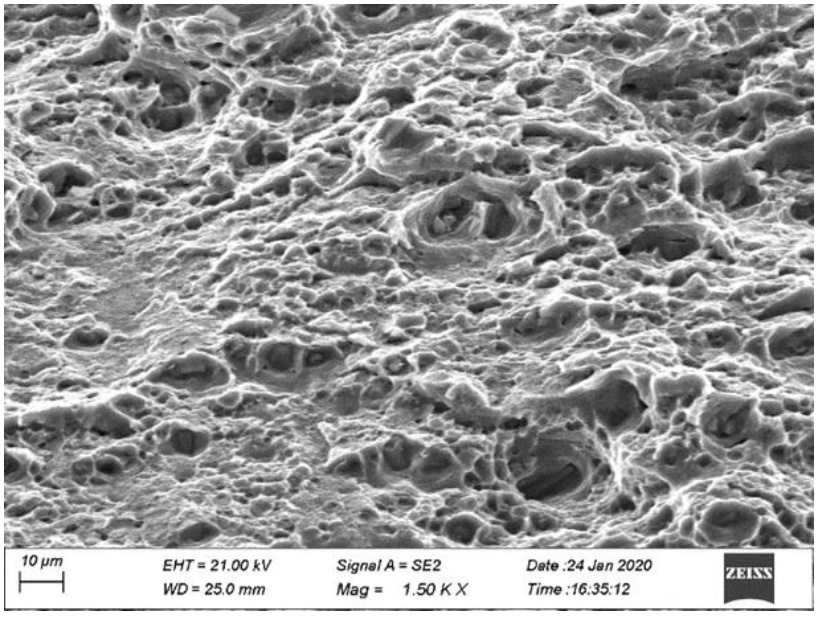

(a)

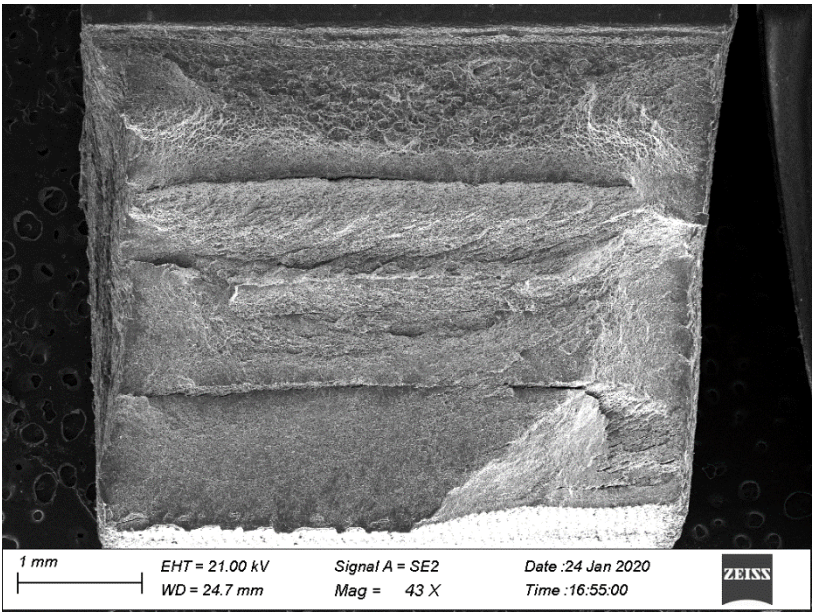
1 mm
EHT = 21.00 kV
WD = 24.7 mm
Signal A = SE2
Mag = 43 X
Date :24 Jan 2020
Time :16:55:00
ZEISS

(b)

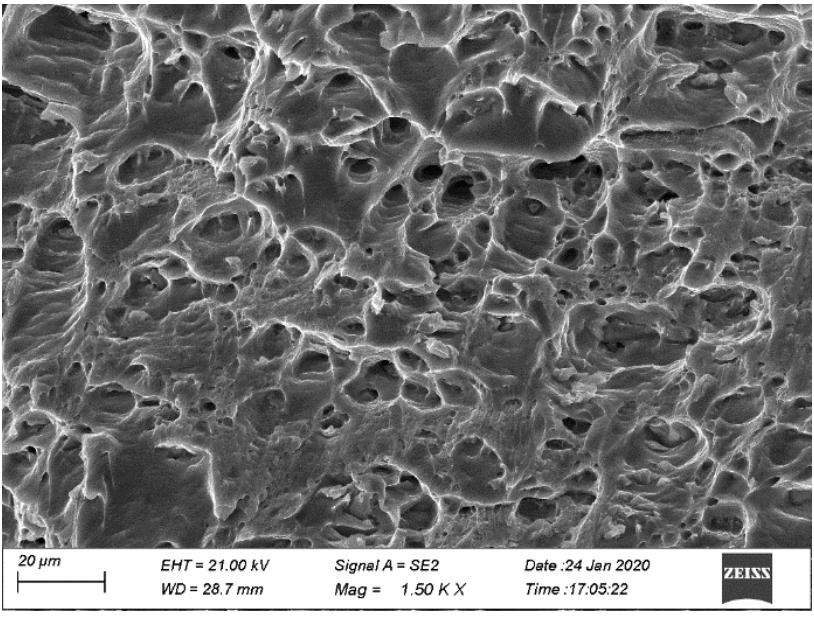
20 µm
EHT = 21.00 kV
WD = 28.7 mm
Signal A = SE2
Mag = 1.50 K X
Date :24 Jan 2020
Time :17:05:22
ZEISS

(c)

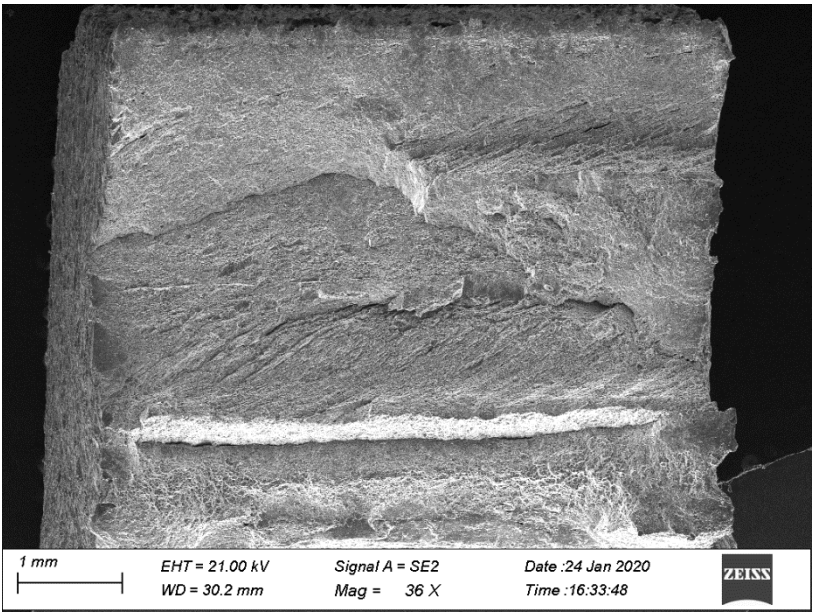

(d)

Fig. 18. SEM images of fracture locations of tensile test specimens (a and b) fracture surface showing dimples and precipitates of specimen welded with TCT (c and d) fracture surface of specimen welded with CST 3.

Conclusions

The aluminum alloy AA 6061 T6 with a thickness of 6 mm is joined using a submerged friction stir welding procedure. In this study, water is used as a cooling medium. The current study illustrates the mathematical modeling necessary to create a stepped pin tool profile and its impact on the mechanical and microstructural characteristics of AA6061-T6 aluminum alloy submerged friction stir welding. The following findings were reached as a result of the current study:

1. From the current design, FSW specimens welded with stepped pin profile tools are free of any defects seen in them.
2. The tool durability index of the tool increases with a decrease in the shoulder to pin diameter (D/d) ratio. A stepped conical pin profile tool has better microscopic and mechanical properties than a standard conical tool because it effectively interacts with the pin and workpiece and has better heat distribution.
3. The stepped conical tool profile with D/d ratio on all five joints with conical pin and stepped pins exhibited significant joints characteristics.
4. The conical stepped tool with the ultimate tensile strength of 245 MPa and joint efficiency of 81 % higher than joints with conical tool pins profile the tensile strength of 237 MPa, joint efficiency of 78.2% of BM. Also, the percentage elongation of the stepped tool shows 15%, which is significant compared with the conical pin of 12.62%.

5. Relatively more refined grains in the nugget zone, a higher microhardness value in the LHDZ zone, and a large contact area between tool and base material were responsible for the stepped tool's effective microstructural and mechanical properties with the stepped tool's effective microstructural the conventional conical tool.

References

[1] R.S. Mishra, Z.Y. Ma: Mater. Sci. Eng. R Reports, 50 (2005) 1–78.
[2] W.M. Thomas, E.D. Nicholas, E.R. Watts, D.G. Staines: Mater. Sci. Forum, 396–402 (2002) 1543–1548.
[3] K. Fuse, V. Badheka: Metals (Basel), 11 (2021) 16.
[4] S. Ji, R. Huang, X. Meng, L. Zhang, Y. Huang: J. Mater. Eng. Perform., 26 (2017) 2359-2367.
[5] Z.Y. Ma: Metall. Mater. Trans. A, 39 (2008) 642–658.
[6] P.J. Ramulu, R.G. Narayanan, S.V. Kailas, J. Reddy: Int. J. Adv. Manuf. Technol., 65 (2013) 1515–1528.
[7] K. Kumar, S.V. Kailas, T.S. Srivatsan: Mater. Manuf. Process., 26 (2011) 915–921.
[8] K.N. Wakchaure, A.G. Thakur, V. Gadakh, A. Kumar: Mater. Today Proc., 5 (2018) 7150–7159.
[9] H. Chen, K. Yan, T. Lin, S. Chen, C. Jiang, Y. Zhao: J. Mater. Sci. Eng. A, 433 (2006) 64–69.
[10] K. Elangovan, V. Balasubramanian:J. Mater. Process. Technol, 200 (2008) 163–175.
[11] A. Kumar, L.S. Raju: Mater. Manuf. Process, 27(2012) 1414–1418.
[12] A. Banik, J. Deb Barma, S.C. Saha: Iran. J. Sci. Technol. - Trans. Mech. Eng, 44 (2020) 749–764.
[13] C.N. Suresha, B.M. Rajaprakash, S. Upadhya: Mater. Manuf. Process, 26 (2011) 1111–1116.
[14] R. Beygi, M.Z. Mehrizi, D. Verdera, A. Loureiro: J. Mater. Process. Technol., 255 (2018) 739–748.
[15] V. Malik, S.V. Kailas: Proc. Inst. Mech. Eng. Part C J. Mech. Eng. Sci, 235 (2021) 744–757.
[16] K. Kumar, S.V. Kailas: Mater. Des, 29 (2008) 791–797.
[17] V. Malik, S.V. Kailas: J. Mater. Process. Technol, 258 (2018) 80-88.
[18] V.S. Gadakh, A. Kumar, G.J.V Patil: Weld. J, 94 (2015) 115S-124S.
[19] S. Ramaiyan, S.K.V. Santhanam, P. Muthuguru: Mater. Res, 21 (2018) 1-9.
[20] P. Prakash, R.S. Anand, S.K. Jha: J. Mech. Sci. Technol, 34 (2020) 289–287.
[21] S.M. Arab, S. Ahmad, J. Jahromi, S.M. Zebarjad: J. Mater. Eng. Perform, 10 (2016) 4587-4597.
[22] R.Z. Xu, S.L. Cui, H. Li, Y.X. Hou, Z.C. Wei: Int. J. Adv. Manuf. Technol, 102 (2019) 3739–3746.
[23] S. Emamian, M. Awang, F. Yusof, P. Hussain, B. Meyghani, A. Zafar: Adv. Join. Technol, Springer Singapore, (2019) 15-37.
[24] E. Salari, M. Jahazi, A. Khodabandeh, H. Ghasemi-Nanesa: Mater. Des, 58 (2014) 381-389.
[25] Y.J. Chao, S. Liu, C.H. Chien: J. Chinese Inst. Eng. Trans. Chinese Inst. Eng. A, 31 (2008) 757–767.
[26] D.M. Neto, P. Neto: Int. J. Adv. Manuf. Technol., 65 (2013) 115–126.

[27] R. Nandan, G. G. Roy, T.J. Lienert, T. Debroy: Acta Mater., 55 (2007) 883–895.
[28] S.D. Ji, Q.Y. Shi, L.G. Zhang, A.L. Zou, S.S. Gao, L.V. Zan: Comput. Mater. Sci., 63 (2012) 218-226.
[29] M.Z.H. Khandkar, J.A. Khan, A.P. Reynolds: Sci. Technol. Weld. Join., 8 (2003) 165–174.
[30] P. Sahlot, A. K. Singh, V.J. Badheka, A. Arora: Trans. Indian Inst. Met., 72 (2019) 1339–1347.
[31] X. Zhu, Y. Chao: J. Mater. Process. Technol., 146 (2004) 263–272.
[32] V.S. Gadakh, K. Adepu: J. Mater. Res. Technol., 2 (2013) 370–375.
[33] D.H. Lammlein, D.R. DeLapp, P. A. Fleming, A.M. Strauss, G. E. Cook: Mater. Des., 30 (2009) 4012–4022.
[34] G. Shinde, R. Arakerimath: Metall. Mater. Eng., 28 (2022) 335–349.
[35] C. Shi, H. Sun, C. Liu, K. Zhu, Q. Yang: Mater. Res. Express, 9 (2022) 056510.
[36] H.I. Khalaf, R. Al-sabur, M.E. Abdullah, A. Kubit, H.A. Derazkola: Materials, 15 (2022) 2223
[37] R.A. Prado, L.E. Murr, K.F. Soto, J.C. McClure: Mater. Sci. Eng. A, 349 (2003) 156–165.
[38] H. Schmidt, J. Hattel: Model. Simul. Mater. Sci. Eng., 13 (2005) 77–93.
[39] A. Arora, M. Mehta, A. De, T. Debroy: Int. J. Adv. Manuf. Technol., 61 (2012) 911–920.
[40] M. Mehta, A. Arora, A. De, T. Debroy: Metall. Mater. Trans. A Phys. Metall. Mater. Sci., 42 (2011) 2716–2722.
[41] J. Zhang, Y. Shen, B. Li, H. Xu, X. Yao, B. Kuang, J. Gao: Mater. Des., 60 (2014) 94-101.
[42] A. Arora, A. De, T. Debroy, A. Arora: Scr. Mater., 64 (2011) 9–12.
[43] T. DebRoy, A. De, H.K.D.H. Bhadeshia, V.D. Manvatkar: Proc. R. Soc. A Math. Phys. Eng. Sci., 468 (2012) 3552–3570.
[44] M. Mehta, G.M. Reddy, A.V. Rao, A. De: Def. Technol., 11 (2015) 229–236.
[45] M. Mehta, A. De, T. DebRoy: Sci. Technol. Weld. Join., 19 (2014) 534–540.
[46] V. Buchibabu, G.M. Reddy, A. De: J. Mater. Process. Technol., 241 (2017) 86-92.
[47] C. Rathinasuriyan, S.K.V. Santhanam: Mater. Res., 21 (2018)
[48] S. Sree Sabari, S. Malarvizhi, V. Balasubramanian: J. Mech. Mater. Eng., 11 (2016) 1–14.
[49] P. Prakash, S.K. Jha, S.P. Lal: Weld. World, 63 (2019) 1531–1546.